Mesh-free simulation of ductile fracture

Bo Cerup Simonsen[1,*,†] and Shaofan Li[2]

[1]*Department of Mechanical Engineering, Maritime Engineering Technical University of Denmark, Denmark*
[2]*Department of Civil Engineering, University of California, Berkeley, U.S.A.*

SUMMARY

This paper is concerned with mesh-free simulations of crack growth in ductile materials, which is a major technical difficulty in computational mechanics. The so-called reproducing kernel particle method, which is a member of the mesh-free method family, is used together with the Gurson–Tvergaard–Needleman constitutive model for simulation of ductile fracture. A study has been carried out to compare the proposed mesh-free simulation with the available experimental results and previous finite element simulations for crack propagation in a three-point-bending steel specimen. The results show that the mesh-free simulation agrees well with experimental results, and it is confirmed that the proposed method provides a convenient and yet accurate means for simulation of ductile fracture. Copyright © 2004 John Wiley & Sons, Ltd.

KEY WORDS: mesh-free method; ductile fracture; crack propagation; Gurson–Tvergaard–Needleman model; experiments

1. INTRODUCTION

There is an enormous application potential for a method for prediction of the onset and propagation of macroscopic cracks in structures undergoing gross plastic deformations. Despite a substantial effort over the past decades, still no method has been proposed which is fully satisfactory with regard to general accuracy on the one hand and ease of use for the engineering society on the other hand. One of the challenges in predicting fracture in structures is the significant span of length scales. While the size of structures is in the order of a meter the mechanics governing material separation under void growth and coalescence is on a scale of 10–100 μm.

The successful prediction of crack propagation requires:

- a criterion that determines when the crack propagates
- a method that can solve the boundary value problem with an evolving crack

---

*Correspondence to: Bo Cerup Simonsen, Department of Mechanical Engineering, Maritime Engineering, Technical
  University of Denmark, Build. 101E, DK-2800 Kgs. Lyngby, Denmark.
†E-mail: bcs@mek.dtu.dk

The classical approach to the first item is fracture mechanics. In the case of small-scale yielding conditions a single parameter (for example the J-integral) gives a satisfactory description of the crack tip conditions. The conventional fracture mechanics—which is obviously very successful—builds on this basis. It breaks down, however, in the presence of excessive plasticity where the fracture toughness turns out to be a strong function of the crack tip constraint—see for example Reference [1] or Reference [2]—which implies that the fracture toughness becomes a function of the size and geometry of the test specimen. So-called two-parameter fracture mechanics (for example J-Q- or J-T theory) has been developed to incorporate the effect of crack tip constraint but although these methods have apparently increased the applicability of the J-approach, [2, 3], they still do not apply to general loading conditions with large strains, large-scale yielding or significant crack growth.

The alternative to fracture mechanics is the so-called local approach. The basic idea is to resolve the continuum mechanics problem all the way to the crack tip and introduce material separation whenever a damage measure has reached a critical value. A very large number of constitutive models with evolving damage have been proposed over the past few decades. The simplest of these methods can be called *damage indicators*. Those methods—for example that of Rice and Tracey [4]—do not include any coupling between the constitutive behaviour and the material damage, except at the point of fracture where the stress carrying capacity is removed instantaneously. A large part of the methods falls in the category of *damage mechanics*, where a scalar or tensor defines the degradation of material stiffness without referring this damage quantity to the microstructure of the material. Finally, yet another category of methods uses micro-mechanics to relate the developing microstructure of the material to the macromechanical behaviour of the material. The model applied in the present paper is based on the idea that material fracture is governed by nucleation, growth and coalescence of voids. The idea was originally proposed by McClintock [5] and Rice and Tracey [4]. It was further developed by Gurson [6] and subsequently modified by Tvergaard and Needleman Tvergaard [7–9] as described later. Although the model has certain shortcomings—see the discussions by Pardoen and Hutchinson [10] and Roychowdhury *et al.* [11] —it has also proved to be able to predict the important phenomena of initiation, [12], and propagation [13]. Since the focus of the present paper is on the application of the mesh-free method rather than on the material model, this so-called Gurson–Tvergaard–Needleman (GTN) model is used here without modifications.

The second challenge mentioned above—solution of the boundary value problem—has also received considerable attention. The most commonly used approach is the finite element method together with an 'element extinction' procedure, see for example Reference [9] or Reference [12]. Once the conditions of the material in an element reach a predefined critical state, the element is taken out of the existing discretization, i.e. the connectivity map is modified to exclude the particular element. With a sufficiently fine discretization and the appropriate constitutive law, this finite element based approach should be able to predict fracture accurately. However, the wide range of physical length scales mentioned earlier and the fact that the crack trajectory is not known *a priori* make it practically impossible to discretize a sufficiently large part of the structure to the scale of the smallest mechanism. Therefore, in practice the finite element models normally need to use a relatively coarse mesh, which introduces problems of mesh size and mesh orientation sensitivity. Various strategies are pursued toward efficient handling of the changing topology, for example adaptive mesh refinement, mesh overlay techniques [14] and discontinuous element formulations [15, 16].

The mesh-free method was initially proposed several decades ago by Lucy [17] and Gingold and Monoghan [18] to study astrophysics problems. Recently, it has experienced a renaissance in solution of problems with which conventional finite element methods may have difficulties such as simulations of crack growth in a solid. Overviews of the mesh-free methods are found in References [19–21]. The mesh-free method used in this paper is the so-called reproducing kernel particle method (RKPM) proposed by Liu *et al.* [22]. The objective of the paper is to illustrate that it is possible to predict ductile fracture by use of the GTN model and the RKPM. The paper describes the basic continuum mechanics formulation used, the special features of the mesh-free interpolant, how the evolving discontinuity is modelled, the theory and implementation of the GTN model and finally a comparison between experiments and predictions of crack propagation in a three-point-bending (TPB) specimen of steel.

Conventional index or tensor notation is used. The summation convention applies to both upper and lower cases. In general, lower case (i, j, k) refer to the components of a tensor and upper case I or J to the identification number of a particle. Parts of the formulation and the notation used here follow that of Belytschko *et al.* [23]. For detailed derivations, for instance of the principle of virtual work, readers are referred to this book.

2. BASIC KINEMATICS

The motion is described in a Cartesian co-ordinate system. In the initial, referential state the position of a material particle is denoted by $\mathbf{X}$. At time t the position is denoted by $\mathbf{x} = \boldsymbol{\varphi}(\mathbf{X}, t)$. Obviously, $\mathbf{X} = \mathbf{x}(\mathbf{X}, 0) = \boldsymbol{\varphi}(\mathbf{X}, 0)$. The displacement of a material point in the time interval from $t = 0$ to t is

$$\mathbf{u}(\mathbf{X}, t) = \boldsymbol{\varphi}(\mathbf{X}, t) - \boldsymbol{\varphi}(\mathbf{X}, 0) = \boldsymbol{\varphi}(\mathbf{X}, t) - \mathbf{X} \tag{1}$$

The velocity is

$$\mathbf{v}(\mathbf{X}, t) = \frac{\partial \boldsymbol{\varphi}(\mathbf{X}, t)}{\partial t} = \frac{\partial \mathbf{u}}{\partial t} = \dot{\mathbf{u}} \tag{2}$$

The deformation gradient is

$$\mathbf{F} = \frac{\partial \boldsymbol{\varphi}(\mathbf{X}, t)}{\partial \mathbf{X}} \tag{3}$$

The velocity gradient is

$$\mathbf{L} = \frac{\partial \mathbf{v}}{\partial \mathbf{x}} = (\nabla \mathbf{v})^{\mathrm{T}} \tag{4}$$

The rate of deformation, $\mathbf{D}$, is the symmetric part of $\mathbf{L}$ and the spin, $\mathbf{W}$, is the skew symmetric part of $\mathbf{L}$, i.e.

$$\mathbf{L} = (\nabla \mathbf{v})^{\mathrm{T}} = \mathbf{D} + \mathbf{W} \tag{5}$$

$$\mathbf{D} = \tfrac{1}{2}(\mathbf{L} + \mathbf{L}^{\mathrm{T}}) \tag{6}$$

$$\mathbf{W} = \tfrac{1}{2}(\mathbf{L} - \mathbf{L}^{\mathrm{T}}) \tag{7}$$

Since a total Lagrangian approach is adopted here, it is convenient to express $\mathbf{D}$ and $\mathbf{W}$ in terms of the reference coordinates. It can be shown that

$$\mathbf{L} = \dot{\mathbf{F}} \cdot \mathbf{F}^{-1} \tag{8}$$

and the rate of deformation and the spin can then be expressed as

$$\mathbf{D} = \tfrac{1}{2}(\dot{\mathbf{F}} \cdot \mathbf{F}^{-1} + \mathbf{F}^{-\mathrm{T}} \cdot \dot{\mathbf{F}}^{\mathrm{T}}) \tag{9}$$

$$\mathbf{W} = \tfrac{1}{2}(\dot{\mathbf{F}} \cdot \mathbf{F}^{-1} - \mathbf{F}^{-\mathrm{T}} \cdot \dot{\mathbf{F}}^{\mathrm{T}}) \tag{10}$$

where $\dot{\mathbf{F}} = \partial \mathbf{v}/\partial \mathbf{X}$.

3. WEAK FORM AND DISCRETIZATION

The total Lagrangian formulation is employed. The weak form can be developed by multiplying the momentum equation by a test function δu_i and integrating over the referential spatial domain:

$$\int_{\Omega_0} \delta u_i \left(\frac{\partial P_{ji}}{\partial X_j} + \rho_0 b_i - \rho_0 \ddot{u}_i \right) \mathrm{d}\Omega_0 = 0 \tag{11}$$

where P_{ij} is the nominal stress, ρ_0 is the initial density of the material, b_i denote the body forces and the domain of integration is the initial (reference) spatial domain Ω_0. The spaces for the trial and test functions are

$$\mathbf{u}(\mathbf{X}, t) \in U \tag{12}$$

$$\delta \mathbf{u}(\mathbf{X}) \in U_0 \tag{13}$$

where U is the space of kinematically admissible displacements and U_0 is the subspace of U for which displacements vanish on displacement boundary conditions. While the trial and test functions used in the conventional finite element method immediately fulfil the requirements of essential boundary conditions, this is not the case for the functions constructed from mesh-free interpolants, such as the smooth particle hydrodynamics (SPH) or the reproducing kernel particle method (RKPM) used here. Special care must therefore be taken to handle essential boundaries so that the requirements given by Equations (12), (13) are met. The procedure described in Reference [24] is used here without modifications for an accurate and well documented treatment of essential boundary conditions. The principle of virtual work can be written as

$$\delta W^{\mathrm{int}}(\delta \mathbf{u}, \mathbf{u}) - \delta W^{\mathrm{ext}}(\delta \mathbf{u}, \mathbf{u}) + \delta W^{\mathrm{kin}}(\delta \mathbf{u}, \mathbf{u}) = 0 \tag{14}$$

where the contributions to the work equation are

$$\delta W^{\mathrm{int}} = \int_{\Omega_0} \delta F_{ij} P_{ji} \, \mathrm{d}\Omega_0 \tag{15}$$

$$\delta W^{\text{ext}} = \int_{\Omega_0} \delta u_i \rho_0 b_i \, \mathrm{d}\Omega_0 + \sum_{i=1}^{n_{\text{SD}}} \int_{\Gamma_{t_i}^0} \delta u_i \bar{t}_i^0 \, \mathrm{d}\Gamma_0 \tag{16}$$

$$\delta W^{\text{kin}} = \int_{\Omega_0} \delta u_i \rho_0 \ddot{u}_i \, \mathrm{d}\Omega_0 \tag{17}$$

where n_{SD} is the number of spatial dimensions, Γ_0 is the boundary with traction boundary conditions and $\bar{t}_i^0$ is the boundary traction. As usual, subscript 0 refers to the initial configuration. The subsequent section will describe in detail how the mesh-free interpolation works. At this point it should be noted that the motion is described by use of discrete, nodal values and interpolation functions as in the finite element method:

$$x_i(\mathbf{X}, t) = x_{iI}(t) N_I(\mathbf{X}) \tag{18}$$

where I denotes the ID-number of a *particle* (equivalent to *node point* in the FEM) and the summation convention works for both upper and lower case indices. The Galerkin method is applied here so the test functions are constructed using the same shape functions as the trial functions. The trial displacement field and the test functions are then, respectively,

$$u_i(\mathbf{X}, t) = u_{iI}(t) N_I(\mathbf{X}) \tag{19}$$

$$\delta u_i(\mathbf{X}, t) = \delta u_{iI}(t) N_I(\mathbf{X}) \tag{20}$$

The velocities and accelerations are found by taking the time derivative of Equation (19):

$$\dot{u}_i(\mathbf{X}, t) = \dot{u}_{iI}(t) N_I(\mathbf{X}) \tag{21}$$

$$\ddot{u}_i(\mathbf{X}, t) = \ddot{u}_{iI}(t) N_I(\mathbf{X}) \tag{22}$$

For the discretized trial and test functions given by Equations (19), (20), it can be shown that the weak form, Equation (14), is equivalent to

$$\delta u_{iI}(f_{iI}^{\text{int}} - f_{iI}^{\text{ext}} + M_{ijIJ}\ddot{u}_{jJ}) = 0 \quad \forall I, i \notin \Gamma_{u_i} \tag{23}$$

where f_{iI}^{int} and f_{iI}^{ext} are the internal and external nodal forces, respectively, M_{kjIJ} is the mass matrix and Γ_{u_i} are the degrees of freedom on the boundary controlled by displacement boundary conditions. The components of internal force, external force and mass matrix are expressed as

$$f_{iI}^{\text{int}} = \int_{\Omega_0} \frac{\partial N_I}{\partial X_j} P_{ji} \, \mathrm{d}\Omega_0 \tag{24}$$

$$f_{iI}^{\text{ext}} = \int_{\Omega_0} N_I \rho_0 b_i \, \mathrm{d}\Omega_0 + \int_{\Gamma_{t_i}^0} N_I \bar{t}_i^0 \, \mathrm{d}\Gamma_0 \tag{25}$$

$$M_{ijIJ} = \delta_{ij} \int_{\Omega_0} \rho_0 N_I N_J \, \mathrm{d}\Omega_0 \tag{26}$$

Finally, since Equation (23) applies for arbitrary values of the nodal displacement components which are not affected directly by essential boundary conditions, it follows that

$$M_{ijIJ}\ddot{u}_{jJ} = f_{iI}^{\text{ext}} - f_{iI}^{\text{int}} \quad \forall I, i \notin \Gamma_{u_i} \tag{27}$$

The weak form, Equation (24) makes use of the nominal stress, which is related to the Cauchy stress and the deformation gradient as

$$\mathbf{P} = J\mathbf{F}^{-1} \cdot \boldsymbol{\sigma} \tag{28}$$

where $J = \det(\mathbf{F})$. Equation (27) is solved by an explicit integration scheme using a central difference method as described in Reference [23].

4. MESH-FREE SIMULATION OF CRACK PROPAGATION

4.1. The RKPM Interpolant

The displacement interpolation in a two-dimensional domain is given by

$$u_i(X_1, X_2) = N_I(X_1, X_2)u_{iI}, \quad i = 1, 2 \text{ and } (X_1, X_2) \in \Omega_0 \tag{29}$$

where u_{iI} is the displacement of particle no. I in the i-direction and $N_I(X_1, X_2)$ is the interpolation function associated with this particle. In the finite element method the trial function approximation within a single element is similar to Equation (29), but the summation would extend only over the nodes of the element containing the material point $\mathbf{X} = (X_1, X_2)$. Most mesh-free interpolations are non-local, i.e. the sampling or the summation is not confined in an element but extends over a much larger, however still limited, spatial area. This property of the finite extent of the interpolant is denoted *compact support* and it conveniently implies that the summation in Equation (29) only has to be carried out over the subset of particles (typically around 20 in 2-D) for which $N_I(X_1, X_2)$ is non-zero.

In this paper the so-called RKPM is used. The RKPM is a further development of the original SPH method [17, 18]. Comprehensive development and application of the method have been performed by the computational mechanics group at Northwestern University, [22–26]. The basic idea of RKPM and the other so-called *corrective SPH* methods is to 'correct' the original SPH kernel (hereafter called window function), $\varphi_\rho(\mathbf{X} - \mathbf{X}_I)$, to make the method a partition of unity so that rigid body motion can be correctly represented. The RKPM not only reproduces a constant but any basis function included in the P_b-vector. The window function $\varphi_\rho(\mathbf{X}_I - \mathbf{X})$ is modified by a factor, the correction function:

$$C_\rho(\mathbf{X} - \mathbf{X}_I) = \mathbf{P}_\text{b}\left(\frac{(\mathbf{X} - \mathbf{X}_I)}{\rho}\right)\mathbf{b}\left(\frac{\mathbf{X}}{\rho}\right) \tag{30}$$

where $\mathbf{P}_\text{b}$ is a vector function of any type and the coefficients held in $\mathbf{b}$ are chosen so that the local truncation error is minimized [22]. The interpolation function is then given by

$$N_I(\mathbf{X}) = \mathbf{P}_\text{b}\left(\frac{(\mathbf{X} - \mathbf{X}_I)}{\rho}\right)\mathbf{b}\left(\frac{\mathbf{X}}{\rho}\right)\varphi_\rho(\mathbf{X} - \mathbf{X}_I)\Delta V_I \tag{31}$$

where ΔV_I is the integration weight of node I. There are various possible choices of both φ_ρ and $\mathbf{P}$. The reproducing property makes it possible to approximate accurately solutions to particular cases—for example a crack tip displacement field as considered by Belytschko *et al.* [27] and Fleming *et al.* [28]. The basis in the present work is composed of polynomials:

$$P_b(X_1, X_2) = (1, X_1, X_2, X_1 X_2) \tag{32}$$

which obviously means that the interpolant can reproduce exactly a bi-linearly varying displacement field (including a constant). The window function is obtained by a Cartesian product of the one-dimensional cubic spline functions:

$$\varphi_\rho(\mathbf{X} - \mathbf{X}_I) = \frac{1}{\rho_1 \rho_2} f_1(X_1 - X_{1I}) f_2(X_2 - X_{2I}) \tag{33}$$

where

$$f_\alpha(X_\alpha - X_{\alpha I}) = \begin{cases} 1 - \frac{2}{3} q_\alpha^2 + \frac{3}{4} q_\alpha^3 & \text{for } 0 \leqslant q_\alpha = \frac{|X_\alpha - X_{I\alpha}|}{\rho_\alpha} < 1 \\ \frac{1}{4}(2 - q_\alpha)^3 & \text{for } 1 \leqslant q_\alpha \leqslant 2 \end{cases} \tag{34}$$

It is seen that this window function has a rectangular support of the size $4\rho_1 \cdot 4\rho_2$ (unit: $[m] \cdot [m]$). The vector $\mathbf{b}(\mathbf{X})$ is found by enforcing the reproducing condition, which leads to the following system of equations:

$$\mathbf{M}(\mathbf{X})\mathbf{b}(\mathbf{X}) = \mathbf{P}_b(\mathbf{0}) \tag{35}$$

where $\mathbf{M}$ is the moment of the window function

$$\mathbf{M}(\mathbf{X}) = \begin{bmatrix} m_{00} & m_{10} & m_{01} & m_{11} \\ m_{10} & m_{20} & m_{11} & m_{21} \\ m_{01} & m_{11} & m_{02} & m_{12} \\ m_{11} & m_{21} & m_{12} & m_{22} \end{bmatrix} \tag{36}$$

The components of the moment matrix are found by a numerical, nodal integration using the trapezoidal rule

$$m_{ij} = \sum \left(\frac{X_1 - X_{1I}}{\rho_1} \right)^i \left(\frac{X_2 - X_{2I}}{\rho_2} \right)^j \varphi_\rho(\mathbf{X} - \mathbf{X}_I) \Delta V_I \tag{37}$$

The integration weights ΔV_I need to be carefully assigned to each node to make the integration correct as discussed in Reference [19]. It should be noted that the correction factor $\mathbf{b}(\mathbf{X})$ is truly a function of $\mathbf{X}$ so it has to be determined at each point where the solution is of interest, i.e. at the particle and Gauss points. Furthermore, for problems like the present one where the topology changes during the solution, $\mathbf{b}(\mathbf{X})$ has to be determined in each time step, at least in the part of the structure affected by the crack.

4.2. Crack Propagation

One of the main challenges in numerical simulations of crack initiation and propagation is that the topology of the structure changes during the deformation process. A practical

G: Gauss Quardrature Points
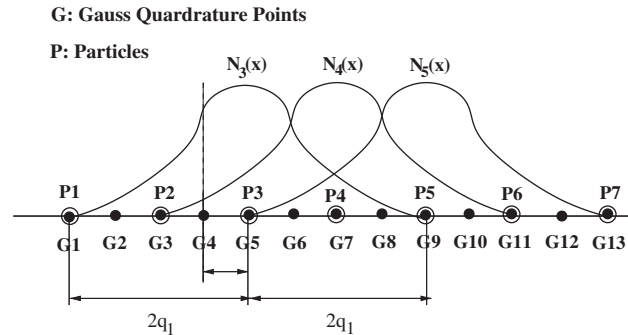
P: Particles

Figure 1. Connectivity in the mesh-free method, one-dimensional case.

solution which has found widespread application in finite element modelling of fracture is the so-called 'erosion', 'element kill' or 'element extinction' method, where an element is taken out of the connectivity matrix once a particular criterion is met. For a sufficiently fine finite element discretization many examples have shown that this method works well—see for example References [9, 12, 29–31]. Despite such examples of success, it is widely recognized that the finite element method is difficult to use for modelling of crack propagation in real-size structures, largely due to the above mentioned problem of the span of length scales. One way of overcoming the problem of resolving the moving crack tip field is to use adaptive meshing. While adaptive meshing has certainly proved efficient in many problems, the method is still complicated to implement and computationally expensive. An alternative to conventional adaptive meshing is to use a highly graded moving overlap grid' which takes the coarse-scale solution to the fine scale [14].

As an alternative to killing elements, it has been proposed to introduce discontinuities into the shape functions of finite elements. This class of methods has shown promising results [15], but it seems that it is still an open question whether the methods work efficiently for ductile fracture, where the shape functions need to include very complex solutions to capture the highly non-linear mechanics at the blunting crack tip.

To alleviate the problems related to the use of an element mesh, a substantial effort has been made to develop the mesh-free method for crack propagation. Since the topology—i.e. the connectivity between material particles—in the mesh-free method is defined differently from that of the finite element method, there is a potential gain with regard to the description and modelling of the propagating crack. Figure 1 illustrates the mesh-free modelling of fracture for a 1-D problem. The locations of Gauss points (GPs) and node points (NPs) are shown together with the support size $2q_1$. The support size of the interpolation function at a NP determines the extent of the integrals in Equations (24)–(26). Assume that GP no. 4 in Figure 1 has reached a state where the material is fully damaged and stresses can no longer be transmitted through the element, i.e. a crack is formed. In the 'erosion' approach used in finite element modelling this would be taken into account by removing the element between NP no. 2 and NP no. 3 from the model. In the present approach the crack is included, i.e. the new topology is enforced, by modifying the domains of the integration in Equations (24)–(26), so that no integral extends over the discontinuity and by updating the shape-functions by use of Equation (35). The domain of integration for NP 3 is then only $X_{GP4} \leqslant X \leqslant X_{NP3} + 2q_1$. This way the
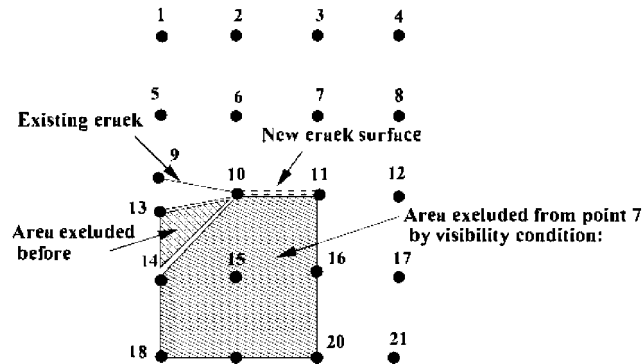
Figure 2. Connectivity and visibility in the mesh-free method, two-dimensional case.

crack edge becomes traction-free which is the correct boundary condition. It should be noted that the mesh-free method conserves mass contrary to the element extinction method.

The same principle can be applied to multiple-dimensional cases, although there is no physically based criteria which can be used to adjust the connectivity map automatically. Several methods have been proposed as discussed in Reference [20]. One of the simplest ways to implement a discontinuity is to use the so-called 'visibility' criterion, [31]. This method has also been applied to three dimensional problems, [32]. The basic idea of this method is that the crack is opaque and that material particles which cannot 'see' each other should not be connected. As an example Figure 2 shows NPs in a model with fairly uniform and isotropic particle distributions. The crack tip is at NP 10 and the equations of motion for NP 7 are considered for the illustration. It is assumed that the interpolation function for NP 7 initially extends over the entire area shown in Figure 2. Consider the case where the deformation is such that the crack tip should be incremented from NP 10 to NP 11. According to the visibility criterion this would exclude the area 'behind' a line connecting NPs 13, 10, 11 and 16 from the domains of integration in Equations (24)–(26) because NP 7 cannot 'see' this area once the crack tip extends to NP 11. As in the previous example the change of model topology obviously calls for a reassignment of integration weights ΔV_I and a recalculation of the model interpolation functions by Equation (35) in the area within the domain of influence of the crack. The visibility criterion introduces discontinuities into the shape-functions wherever a domain of influence is partially cut by a discontinuity, i.e. at the crack tip, see Reference [20]. From a theoretical point of view this is quite unsatisfactory because it violates the foundation of the Galerkin method. In particular it is unfortunate that the potential inaccuracy is introduced exactly at the crack tip, where the stress and deformation state has to be carefully evaluated in order to propagate the crack correctly. On the other hand the solution at the crack tip comes as a sum of several contributions, and it is not immediately clear how the discontinuities of the individual shape-functions affect the total solution. In the application examples given at the end of the paper it is shown that the field at the crack tip is rather smooth, so without further investigation into accuracy and convergence aspects, it is assumed here that the visibility criterion can be practically used for problems of ductile fracture like the ones considered in this paper.

The crack propagation procedure is implemented in the following way:

1. An initial crack is defined as a line extending between an arbitrary point in space and a particle (for example NP no. 10 in Figure 2).
2. The connectivity between particles and Gauss points is defined by search routines with due consideration to the 'crack line(s)'. This search is performed in the initial, reference configuration.
3. The system of equations, Equation (27), is set up and the solution is incremented using explicit integration in time.
4. The material damage is evaluated in the particles around the crack tip.
5. If the damage has reached a critical magnitude at a particle ahead of the crack, then

    - the 'crack line' is extended to this particle, which is at the new crack tip.
    - a new particle is introduced in the location of the previous crack tip particle and this new particle inherits all historical data of the old particle. The two particles at the previous crack tip share the original integration weight equally. Finally these two particles are separated by a distance which is small compared to the spacing of the particles.
    - the procedure is continued from step 2 above.

    If no critical damage state is reached ahead of the crack tip, the procedure is continued from step 3.

During the solution, the geometry of the crack is recorded as a list of line segments connecting particles.

5. CONSTITUTIVE MODELLING

The first part of this section describes the theoretical background to the so-called Gurson–Tvergaard–Needleman (GTN) model and derives the set of governing non-linear equations. The last part of the section describes how the equations are solved by implicit integration. The derivation largely follows the method of Aravas [33], however, modified to be consistent with the present rate formulation, somewhat as in Reference [34].

5.1. The Gurson–Tvergaard–Needleman Material Model

The rate of deformation tensor $\mathbf{D}$ is decomposed into additive elastic and plastic parts:

$$\mathbf{D} = \mathbf{D}^{\text{el}} + \mathbf{D}^{\text{pl}} \tag{38}$$

The Jaumann rate of the Cauchy stress $\boldsymbol{\sigma}$ is used in the present hypoelastic formulation:

$$\boldsymbol{\sigma}^{\nabla J} = \mathbf{C} : \mathbf{D}^{\text{el}} = \mathbf{C} : (\mathbf{D} - \mathbf{D}^{\text{pl}}) = \boldsymbol{\sigma}^{\text{el}} - \mathbf{C} : \mathbf{D}^{\text{pl}} \tag{39}$$

where

$$C_{ijkl} = 2G\delta_{ik}\delta_{jl} - \left(K - \tfrac{2}{3}G\right)\delta_{ij}\delta_{kl} \tag{40}$$

and the shear and bulk moduli are

$$G = \frac{E}{2(1+v)} \tag{41}$$

$$K = \frac{E}{3(1-2v)} \tag{42}$$

The trial stress is computed by taking into account the effect of finite rotation, which is accomplished by using the Hughes–Winget formula [35].

$$\boldsymbol{\sigma}_{n+1}^{\text{el}} = \mathbf{Q}\boldsymbol{\sigma}_n\mathbf{Q}^{\text{T}} + \Delta t \mathbf{C}^{\nabla J} : \mathbf{D} \tag{43}$$

$$\mathbf{Q} = \mathbf{I} + (\mathbf{I} - \alpha\mathbf{W})^{-1}\mathbf{W} \tag{44}$$

where $\alpha = 0.5$. It should be noted that the global integration scheme assumes constant first-order derivatives throughout the time step, which is consistent with the above assumption of constant values of $\mathbf{Q}$ and $\mathbf{W}$ during the time step. The hydrostatic, deviatoric and equivalent stresses are defined as follows:

$$\sigma_m = \tfrac{1}{3}\boldsymbol{\sigma} : \mathbf{I} \tag{45}$$

$$\boldsymbol{\sigma}_{\text{dev}} = \boldsymbol{\sigma} - \sigma_m\mathbf{I} \tag{46}$$

$$\sigma_{\text{eq}} = \left(\tfrac{3}{2}\boldsymbol{\sigma}_{\text{dev}} : \boldsymbol{\sigma}_{\text{dev}}\right)^{1/2} \tag{47}$$

The stress tensor can then be decomposed as

$$\boldsymbol{\sigma} = \sigma_m\mathbf{I} + \tfrac{2}{3}\sigma_{\text{eq}}\mathbf{n} \tag{48}$$

where

$$\mathbf{n} = \frac{3}{2\sigma_{\text{eq}}}\boldsymbol{\sigma}_{\text{dev}} \tag{49}$$

The inelastic behaviour of the material is described by a plasticity model which includes void growth caused by hydrostatic tension. The Gurson model used in this paper is the computational version proposed by Tvergaard and Needleman [9], which has been extensively used in numerical simulations and has been commonly referred to as the Gurson–Tvergaard–Needleman (GTN) model. The basic idea is that the state of the material damage is described by the current void volume fraction f, i.e. the volume of voids to the total element volume in a representative volume element. The material between the voids, i.e. at the microscopic level, is assumed to follow a general, isotropic material hardening law $f_h(\bar{\varepsilon}^{\text{pl}})$ where $\bar{\varepsilon}^{\text{pl}}$ is the microscopic, work-equivalent plastic strain. In the numerical computations shown later, f_h is described by a power law, i.e.

$$\bar{\sigma}_0 = f_h(\bar{\varepsilon}^{\text{pl}}) \tag{50}$$

$$= \sigma_y\left(1 - \frac{E}{\sigma_y}\bar{\varepsilon}^{\text{pl}}\right)^{\text{N}} \tag{51}$$

where σ_y is the initial yield stress. The evolution of $\bar{\varepsilon}^{\mathrm{pl}}$ is determined from the condition that the plastic work of the macroscopic stresses and strains should be equal to the energy dissipated in plastic deformations at the microlevel:

$$(1-f)\bar{\sigma}_0\dot{\bar{\varepsilon}}^{\mathrm{pl}} = \boldsymbol{\sigma}:\mathbf{D}^{\mathrm{pl}} \tag{52}$$

which leads to

$$\dot{\bar{\varepsilon}}^{\mathrm{pl}} = \frac{\boldsymbol{\sigma}:\mathbf{D}^{\mathrm{pl}}}{(1-f)\bar{\sigma}_0} \tag{53}$$

At the macrolevel, the yield function, or the flow potential, is given as

$$\Phi = \left(\frac{\sigma_{\mathrm{eq}}}{\bar{\sigma}_0}\right)^2 + 2q_1 f^*(f)\cosh\left(\frac{3q_2\sigma_m}{2\bar{\sigma}_0}\right) - (1 + q_1^2 f^*(f)^2) \tag{54}$$

It is seen that when the damage parameter f (the volume fraction of voids) is zero the Gurson model reduces to J_2 flow theory. The parameters q_1 and q_2 were introduced by Tvergaard [7, 8], to bring predictions of the original Gurson model [6], into closer agreement with full numerical analyses of a periodic array of voids. The function $f^*(f)$ was proposed by Tvergaard and Needleman [9], to account for the effects of rapid void coalescence at failure.

$$f^*(f) = \begin{cases} f & \text{for } f \leqslant f_c \\ f_c + \frac{1/q_1 - f_c}{f_f - f_c}(f - f_c) & \text{for } f_c < f \leqslant f_f \\ 1/q_1 & \text{for } f > f_f \end{cases} \tag{55}$$

The void volume grows partly due to the expansion of existing voids and partly due to the nucleation of new voids:

$$\dot{f} = \dot{f}_{\mathrm{growth}} + \dot{f}_{\mathrm{nucleation}} \tag{56}$$

Since the material between the voids is incompressible, the growth rate of existing voids is

$$\dot{f}_{\mathrm{growth}} = (1-f)\mathbf{D}^{\mathrm{pl}}:\mathbf{I} \tag{57}$$

Nucleation of voids has previously been considered to be either stress or strain controlled. In the present work only strain controlled nucleation is considered in the form

$$\dot{f}_{\mathrm{nucleation}} = A_{\mathrm{N}}\dot{\bar{\varepsilon}}^{\mathrm{pl}} \tag{58}$$

The formulation proposed by Chu and Needleman [36] is used, i.e. the nucleation strain follows a normal distribution with a mean value ε_n and a standard deviation s_{N}:

$$A_{\mathrm{N}}(\bar{\varepsilon}^{\mathrm{pl}}) = \frac{f_{\mathrm{N}}}{s_{\mathrm{N}}\sqrt{2\pi}}\exp\left[-\frac{1}{2}\left(\frac{\bar{\varepsilon}^{\mathrm{pl}} - \varepsilon_{\mathrm{N}}}{s_{\mathrm{N}}}\right)^2\right] \tag{59}$$

where f_{N} is the volume fraction of void nucleating particles.

As discussed by various authors, for example Tvergaard [37], Pardoen and Hutchinson [10] and Dodds *et al.* [11, 38] the macroscopic material behaviour during void initiation, growth and coalescence may exhibit a sensitivity to the shape and distribution of voids which cannot

be captured by the void volume fraction alone. Even if the predicted value of f may not correspond to the measured value, several studies have shown that the model has excellent capacity to predict macroscopic behaviour, i.e. crack length, applied loads, etc. Reference is made to Yu [39], Mathur *et al.* [29], Besson *et al.* [12] and Baaser and Gross [30], Xia *et al.* [13, 40, 41], for various examples ranging from small specimens to large-scale shell structures. It is seen from Equation (54) that as the void volume fraction, f, grows towards f_f and $f^*(f)$ approaches $1/q_1$, the yield surface for the macroscopic stresses shrinks towards a point. To attain numerical stability the present procedure assumes full material damage, i.e. $\boldsymbol{\sigma} = \mathbf{0}$, when $f = k_f f_f$ where $0.5 < k_f < 0.9$, as discussed later. The flow rule gives

$$\mathbf{D}^{\mathrm{pl}} = \dot{\lambda} \frac{\partial \Phi}{\partial \boldsymbol{\sigma}} \tag{60}$$

$$= \dot{\lambda} \left\{ \frac{1}{3} \frac{\partial \Phi}{\partial \sigma_m} \mathbf{I} + \frac{\partial \Phi}{\partial \sigma_{\mathrm{eq}}} \mathbf{n} \right\} \tag{61}$$

Define

$$D_m = \dot{\lambda} \left(\frac{\partial \Phi}{\partial \sigma_m} \right) \tag{62}$$

$$D_{\mathrm{eq}} = \dot{\lambda} \left(\frac{\partial \Phi}{\partial \sigma_{\mathrm{eq}}} \right) \tag{63}$$

and use these definitions in Equation (61). The flow rule then finally writes

$$\mathbf{D}^{\mathrm{pl}} = \tfrac{1}{3} D_m \mathbf{I} + D_{\mathrm{eq}} \mathbf{n} \tag{64}$$

Elimination of $\dot{\lambda}$ from Equations (62), (63) gives

$$D_m \frac{\partial \Phi}{\partial \sigma_{\mathrm{eq}}} + D_{\mathrm{eq}} \frac{\partial \Phi}{\partial \sigma_m} = 0 \tag{65}$$

By inserting Equation (64) back into Equation (39) and integrating from t_n to t_{n+1} it can be shown that the relaxation from the trial stress is given by

$$\boldsymbol{\sigma}_{n+1} = \boldsymbol{\sigma}^{\mathrm{el}} - K \Delta t D_m \mathbf{I} - 2 G \Delta t D_{\mathrm{eq}} \mathbf{n}_{n+1} \tag{66}$$

The mean and equivalent components of Equation (66) are

$$\sigma_m = \sigma_m^{\mathrm{el}} - \Delta t K D_m \tag{67}$$

$$\sigma_{\mathrm{eq}} = \sigma_m^{\mathrm{el}} - 3 \Delta t G D_{\mathrm{eq}} \tag{68}$$

The underlying assumption of constant values of D_m and D_{eq} during the time step is consistent with the global, explicit integration method, as mentioned.

As noted by Aravas, Equation (66) shows that the return in the deviatoric stress space is along $\mathbf{n}_{n+1}$ which can be determined from the trial stress tensor:

$$\mathbf{n}_{n+1} = \frac{3}{2\sigma_{eq}^{el}} \, \boldsymbol{\sigma}_{dev}^{el} \tag{69}$$

The fact that $\mathbf{n}_{n+1}$ is determined by the elastic trial stress tensor simplifies the analysis significantly because the stress tensor at t_{n+1} is then determined by only two unknowns, (D_m, D_{eq}), instead of all six components of the stress tensor.

5.2. Constitutive Update

Given the stress tensor $\boldsymbol{\sigma}_n$ at time t_n, the time step size Δt and the rate of deformation tensor $\mathbf{D}$, the task is to calculate the stress $\boldsymbol{\sigma}_{n+1}$ at time t_{n+1}. In the previous section it was shown that the non-linear set of equations defining the stress state at t_{n+1} can be set up to be a function of only the two unknowns D_m and D_{eq}. In summary this set of equations is

1. The yield function, Equation (54).
2. The associative flow rule, Equation (65).
3. The stress state at t_{n+1} expressed in terms of D_m and D_{eq}, Equation (66)
4. The evolution of state variables, Equations (53), (56).

The two internal variables, the effective plastic strain and the void volume fraction, define the state of the material and are kept as the vector H, i.e.

$$H_1 = \bar{\varepsilon}^{pl} \tag{70}$$

$$H_2 = f \tag{71}$$

The time derivatives of these state variables are given by Equations (53), (56):

$$h_1 = \frac{\partial H_1}{\partial t} = \frac{\sigma_m \mathbf{D}_m + \sigma_{eq} \mathbf{D}_{eq}}{(1-f)\sigma_0} \tag{72}$$

$$h_2 = \frac{\partial H_2}{\partial t} = (1-f)\mathbf{D}_m + A_N \dot{\bar{\varepsilon}}^{pl} \tag{73}$$

$$= (1-f)\mathbf{D}_m + A_N h_1 \tag{74}$$

The integration in time is then simply given by

$$H_{1,n+1} = H_{1,n} + \Delta t h_1 \tag{75}$$

$$H_{2,n+1} = H_{2,n} + \Delta t h_2 \tag{76}$$

In order to determine the values of D_m and D_{eq} which satisfy the yield function and the flow rule at t_{n+1} an iterative Newton method is used. The two equations, Equations (65), (54),

to be solved are denoted f_1 and f_2, respectively:

$$f_1(D_m, D_{eq}) = D_m \frac{\partial \Phi}{\partial \sigma_{eq}} + D_{eq} \frac{\partial \Phi}{\partial \sigma_m} = 0 \tag{77}$$

$$f_2(D_m, D_{eq}) = \Phi(D_m, D_{eq}) = 0 \tag{78}$$

where the $n + 1$ subscript is dropped for simplicity. The roots (D_m, D_{eq}) are determined in a predict-correct iteration by improving the initial, predicted estimate, (D_m^k, D_{eq}^k)

$$D_m^{k+1} = D_m^k + \Delta D_m^k \tag{79}$$

$$D_{eq}^{k+1} = D_{eq}^k + \Delta D_{eq}^k \tag{80}$$

where k is an iteration counter. The correction $(\Delta D_m^k, \Delta D_{eq}^k)$ is found by a first-order Taylor expansion of f_1 and f_2 and solution of the resulting linearized set of equations:

$$f_1^{k+1} = f_1^k + \frac{\partial f_1^k}{\partial D_m} \Delta D_m^k + \frac{\partial f_1^k}{\partial D_{eq}} \Delta D_{eq}^k = 0 \tag{81}$$

$$f_2^{k+1} = f_2^k + \frac{\partial f_2^k}{\partial D_m} \Delta D_m^k + \frac{\partial f_2^k}{\partial D_{eq}} \Delta D_{eq}^k = 0 \tag{82}$$

where the notion $f_i^k = f_i(D_m^k, D_{eq}^k)$ is used. Appendices A and B summarize the iteration scheme and list the involved partial derivatives.

6. NUMERICAL EXAMPLE AND DISCUSSIONS

Prior to simulation of ductile fracture, to validate our formulation and computer code, we first conducted a numerical simulation of pre- and post-necking based on J-2 plasticity. Comparisons to the results presented by Mikkelsen [42] showed that the presently used mesh-free method gave the same results as presented by Mikkelsen to an accuracy within the read-off error of the graphs in that paper.

To discuss and demonstrate the predictive power of the proposed method for simulation of crack propagation under ductile conditions, our mesh-free simulations focus on a three-point-bending test, whose experimental data is well documented [43, 44], and has been used as a benchmark test in finite element simulations by Xia *et al.* [40]. In the computational procedure proposed by Xia *et al.*, the crack path is pre-defined to be within a row of the so-called 'computational cells', each with a constitutive behaviour according to the GTN model, described in the present paper. Xia *et al.* choose a side length of the computational cells of 0.2 mm and adjusted the material parameters of the GTN model to give a good prediction of the loads and crack growth in the TPB specimen. To make the present predictions easily comparable to those of Xia *et al.*, the present work also uses particle spacing of 0.2 mm around the expected path of the crack and uses the same material parameters as found by Xia *et al.* The test specimen dimensions and material parameters are given in Table I.

Table I. Specimen dimensions and material parameters.

Total length, L [mm]	220
Distance btwn. supports, H [mm]	200
Width, W [mm]	50
Initial notch depth, a_0 [mm]	30
Thickness*, B [mm]	25.4
Elastic modulus, E [GPa]	200
Poisson ratio, v [1]	0.3
Initial yield stress, σ_y, Equation (51), [MPa]	400
Hardening exponent, N, Equation (51), [1]	10
Initial void volume ratio, f [1]	0.005
Void volume at coalescence, f_C, Equation (55), [1]	0.021
Void volume at total failure, f_f, Equation (55), [1]	0.2109
GTN parameters, (q_1, q_2), Equation (54)	(1.5,1)
Void nucleation parameter, f_N, Equation (59) [1]	0

*Note: The specimen thickness, B, is only used to transfer the measured load to a load per unit thickness, P, in the 2-D space.

Symmetry conditions are not enforced, in order to allow the crack to move away from the symmetry line. The model initially consists of 8399 particles and this number increases to 8427, as the crack length increases 5.6 mm during the process. There are 8539 background cells in the mesh-free discretization. Each of them contains four Gauss quadrature points for the numerical integration of Equations (24)–(26). The need for a small particle spacing at the crack tip relative to the specimen dimensions makes it necessary to use a graded mesh. Since the convergence of mesh-free interpolation requires a quasi-uniform particle distribution, a highly graded background grid is needed to ensure that each Gauss point is covered by supports of an appropriate number of interpolation functions. The essential boundary conditions are prescribed by forcing displacement at the boundary in a simple but rather crude manner: Each of the two support points are fixed by prescribing the displacement at the two particles occupying the appropriate positions, whereas the essential boundary condition at the loading point is prescribed by specifying a uniform displacement over the neighbouring 13 densely spaced particles to assure a global bending mode of the beam rather than just a local indentation at the loading point. The displacement of the loading point is increased at a sufficiently low and smooth rate to ensure that dynamic effects do not dominate the response.

Figure 3 shows the void volume fraction and the vertical stress ahead of the crack tip. It is seen that the maximum void growth occurs ahead of the crack tip. Due to numerical difficulties when the void volume fraction is close to f_f, the present routine assumes full material damage when $f = k_f f_f$, with $k_f = 0.5$. It is seen from Figure 3 that the vertical stress, σ_{22} diminishes a distance of approximately one to two particle spacings ahead of the tip. This effect of stress reduction due to material damage smoothes the discontinuous 'cutting' process and the solution becomes rather insensitive to the chosen value of k_f. Figure 4 shows sequences of the global bending of the beam together with close-ups of the area around the crack tip. The close-ups show that the load does introduce some local indentation but the figures also illustrate that the global bending is dominant, as it should be. Figure 5 shows a comparison between the present predictions and the experiments by Joyce and Hacket and Joyce and Link as published by Xia et al. [40]. There is seen to be a good agreement between experiments and theory, with an agreement equivalent to the results presented by Xia et al. [40], where a finite element
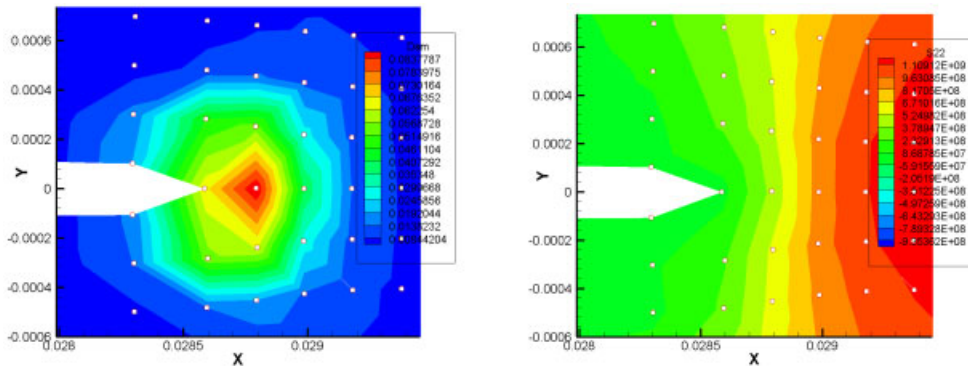
Figure 3. The void volume fraction, f, and the stress $\sigma_{22} = \sigma_{yy}$ at the crack tip before any crack tip propagation has taken place.

method was used. As the purpose of the paper is to demonstrate that the mesh-free method can be used to predict ductile fracture and give similar results to the FEM, no attempts have been made here at carefully adjusting material- and numerical parameters to make a perfect fit to experiments. Figure 6 shows the predicted increase in crack length as a function of the displacement of the loading point. The experimental results presented by Xia *et al*. [40], also showed a crack length of approximately 5 mm when the displacement was 6.5 mm, i.e. a result very close to the theoretical prediction shown in Figure 6.

7. CONCLUSION

The objective of this paper is to present a numerical model for prediction of crack propagation in ductile metals. Plane strain is assumed to model the crack tip condition. The basic framework is the mesh-free method, the Reproducing kernel particle method, which represents a further development of the SPH Method. The Gurson–Tvergaard–Needleman model is adopted as the constitutive model. The evolving topology is modelled by use of the so-called visibility criterion. The validity of this criterion may be questioned because it may introduce discontinuities around the crack tip. However, the numerical computations presented here show that the proposed method seems to work well for the present problem of ductile crack propagation. A careful comparison study was conducted for crack propagation in a three-point-bending (TPB) specimen to compare mesh-free simulation with experimental data [43, 44] and the results of finite element computation previously obtained by Xia *et al*. [40] via a so-called computational cell model (homogenization model). This study shows that the results of the proposed mesh-free method are in good agreement with the previously published experimental and numerical results.

The proposed methodology could be further developed along various natural paths:

- Development of the crack description so that it is not restricted to evolving from node to node. It could easily be developed to evolve from Gauss point to Gauss point or it could advance more continuously between the Gauss Points.
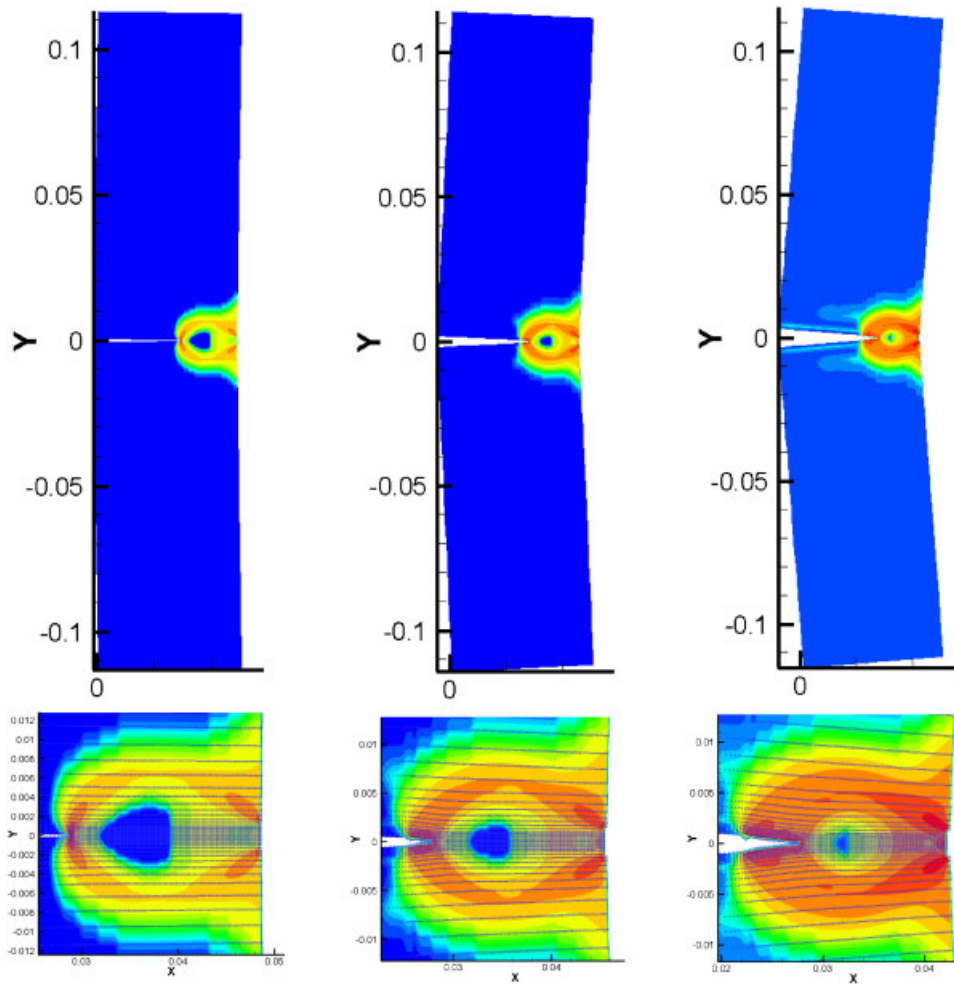
Figure 4. Sequences of the TPB process. Δ: Displacement of loading point. Δa:
Increase of crack length. Left: $\Delta = 1.5$ mm, $\Delta a = 0$. Middle: $\Delta = 4.6$ mm,
$\Delta a = 2.4$ mm. Right: $\Delta = 7.8$ mm, $\Delta a = 5.6$ mm.

- Development of a procedure where crack initiation can also be modelled, i.e. a crack can develop in a body which is initially crack-free.
- Coupling with the finite element method so that the mesh-free modelling is only used around the crack tip.
- Extension to 3-D.

It is thus believed that the proposed methodology could be further developed to become an accurate and practical procedure for modelling of ductile crack propagation.
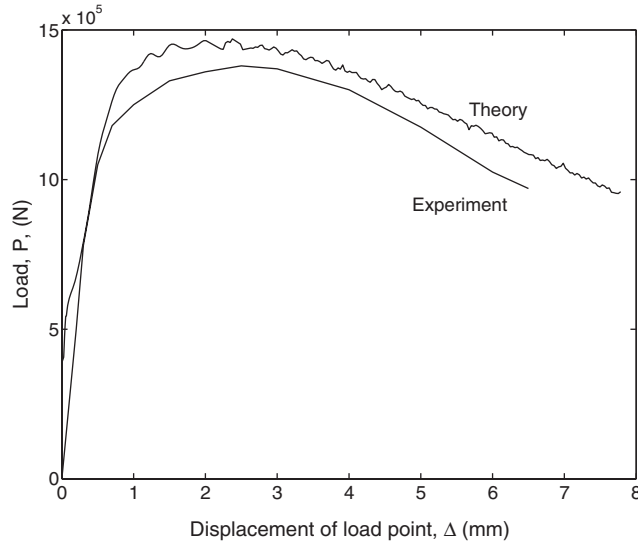
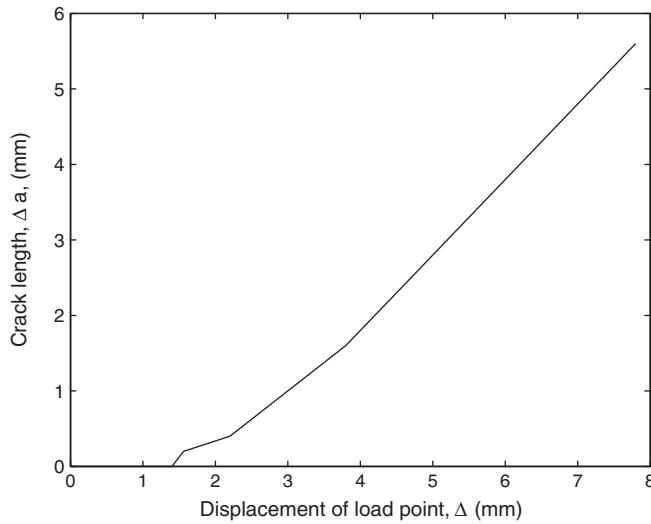Figure 5. Predicted and measured load vs displacement in the TPB tests.

Figure 6. Predicted increase in crack length vs displacement in the TPB tests.

APPENDIX A: STRESS UPDATE ALGORITHM

A.1. Summary of calculation procedure

Equations (81), (82) can be written as

$$
\begin{bmatrix} \Delta D_m^k \\ \Delta D_{\mathrm{eq}}^k \end{bmatrix} = \begin{bmatrix} K_{11} & K_{12} \\ K_{21} & K_{22} \end{bmatrix}^{-1} \begin{bmatrix} R_1 \\ R_2 \end{bmatrix}
\tag{A1}
$$

where the coefficients K_{ij} and R_i are the partial derivatives of f_i and the residuals respectively, as derived below.

If plasticity is detected from the trial stress tensor, i.e. $\Phi > 0$, then the following iterative scheme determines the stress at the end of the time step.

1. Set the iteration counter $k = 0$
2. Initialize. If $t = 0$ then

$$D_m = D_{\text{eq}} = 0 \tag{A2}$$

$$\dot{H}_1 = \dot{H}_2 = 0 \tag{A3}$$

otherwise use the values of the previous time step:
3. Calculate K_{ij}, see below.
4. Calculate R_i, see below.
5. Invert K_{ij} and get the increments in the solution vector from Equation (A1).
6. Update the solution

$$D_m^{k+1} = D_m^k + \Delta D_m \tag{A4}$$

$$D_{\text{eq}}^{k+1} = D_{\text{eq}}^k + \Delta D_{\text{eq}} \tag{A5}$$

$$\sigma_m^{k+1} = \sigma_m^e - K \Delta t D_m^{k+1} \tag{A6}$$

$$\sigma_{\text{eq}}^{k+1} = \sigma_{\text{eq}}^e - 3G \Delta t D_{\text{eq}}^{k+1} \tag{A7}$$

$$\dot{H}_1^{k+1} = \dot{\bar{\varepsilon}}^p = \frac{\sigma_m^{k+1} D_m^{k+1} + \sigma_{\text{eq}}^{k+1} D_{\text{eq}}^{k+1}}{(1-f)\bar{\sigma}_0} \tag{A8}$$

$$\dot{H}_2^{k+1} = \dot{f} = (1-f)(D_m \mathbf{I} + D_{\text{eq}} \mathbf{n}) \tag{A9}$$

$$+ A \frac{\sigma_m D_m + \sigma_{\text{eq}} D_{\text{eq}}}{(1-f)\bar{\sigma}_0} \tag{A10}$$

$$A = \frac{f_N}{s_N \sqrt{2\pi}} \exp\left[-\frac{1}{2}\left(\frac{\bar{\varepsilon}^p - \varepsilon_N}{s_N}\right)^2\right] \tag{A11}$$

$$H_{1,n+1}^{k+1} = H_{1,n} + \Delta t \dot{H}_1^{k+1} \tag{A12}$$

$$H_{2,n+1}^{k+1} = H_{2,n} + \Delta t \dot{H}_2^{k+1} \tag{A13}$$

7. Check convergence. Converged if $|f_1| < \varepsilon_1$ and $|f_2| < \varepsilon_2$ where $\varepsilon_1 = \varepsilon_2 = 10^{-10}$ is used. If not converged set $k = k + 1$ and return to 3. If converged, then compute the stresses as:

$$\boldsymbol{\sigma}_{n+1} = \boldsymbol{\sigma}^e - \Delta t(K D_m \mathbf{I} + 2G D_{\text{eq}} \mathbf{n}) \tag{A14}$$

A.2 Coefficients in the newton method

The constants K_{ij} and R_i in Equation (A1) are

$$K_{11} = \frac{\partial f_1(D_m, D_{\text{eq}})}{\partial D_m}$$

$$= \frac{\partial \Phi}{\partial \sigma_{\text{eq}}} + D_m \left(-\Delta t K \frac{\partial^2 \Phi}{\partial \sigma_{\text{eq}} \partial \sigma_m} + \sum_{i=1}^{2} \frac{\partial^2 \Phi}{\partial \sigma_{\text{eq}} \partial H_i} \frac{\partial H_i}{\partial D_m} \right)$$

$$- D_{\text{eq}} \left(-\Delta t K \frac{\partial^2 \Phi}{\partial \sigma_m^2} + \sum_{i=1}^{2} \frac{\partial^2 \Phi}{\partial \sigma_m \partial H_i} \frac{\partial H_i}{\partial D_m} \right) \tag{A15}$$

$$K_{12} = \frac{\partial f_1(D_m, D_{\text{eq}})}{\partial D_{\text{eq}}}$$

$$= -\frac{\partial \Phi}{\partial \sigma_m} + D_m \left(-3G\Delta t \frac{\partial^2 \Phi}{\partial \sigma_{\text{eq}}^2} + \sum_{i=1}^{2} \frac{\partial^2 \Phi}{\partial \sigma_{\text{eq}} \partial H_i} \frac{\partial H_i}{\partial D_{\text{eq}}} \right)$$

$$- D_{\text{eq}} \left(-3G\Delta t \frac{\partial^2 \Phi}{\partial \sigma_m \partial \sigma_{\text{eq}}} + \sum_{i=1}^{2} \frac{\partial^2 \Phi}{\partial \sigma_m \partial H_i} \frac{\partial H_i}{\partial D_{\text{eq}}} \right) \tag{A16}$$

$$K_{21} = \frac{\partial f_2(D_m, D_{\text{eq}})}{\partial D_m}$$

$$= -\Delta t K \frac{\partial \Phi}{\partial \sigma_m} + \sum_{i=1}^{2} \frac{\partial \Phi}{\partial H_i} \frac{\partial H_i}{\partial D_m} \tag{A17}$$

$$K_{22} = \frac{\partial}{\partial D_{\text{eq}}} \phi_2(D_m, D_{\text{eq}})$$

$$= -3G\Delta t \frac{\partial \Phi}{\partial \sigma_{\text{eq}}} + \sum_{i=1}^{2} \frac{\partial \Phi}{\partial H_i} \frac{\partial H_i}{\partial D_{\text{eq}}}$$

$$R_1 = -f_1(D_m, D_{\text{eq}})$$

$$= -D_m \frac{\partial \Phi}{\partial \sigma_{\text{eq}}} + D_{\text{eq}} \frac{\partial \Phi}{\partial \sigma_m}$$

$$R_2 = -f_2(D_m, D_{\text{eq}})$$

$$= -\Phi(\sigma_m, \sigma_{\text{eq}}, H_1, H_2)$$

In the derivations of the above results it has been used that

$$\frac{\partial \sigma_m}{\partial D_{\text{eq}}} = 0$$

$$\frac{\partial \sigma_m}{\partial D_m} = -K\Delta t$$

$$\frac{\partial \sigma_{\text{eq}}}{\partial D_{\text{eq}}} = -3G\Delta t$$

$$\frac{\partial \sigma_{\text{eq}}}{\partial D_m} = 0$$

which follows directly from Equations (67), (68). The partial derivatives necessary for the evaluation of the above coefficients are given below.

A.3 Derivatives of the GTN model

$$\Phi = \left(\frac{\sigma_{\text{eq}}}{\sigma_y}\right)^2 + 2q_1 f^*(f) \cosh\left(\frac{3q_2\sigma_m}{2\sigma_y}\right) - (1 + (q_1 f^*(f))^2)$$

$$H_1 = \bar{\varepsilon}^{\text{pl}}$$

$$H_2 = f$$

$$\frac{\partial \Phi}{\partial \sigma_m} = \frac{3q_1 q_2 f^*(f)}{\bar{\sigma}_0} \sinh\left(\frac{3q_2\sigma_m}{2\sigma_y}\right)$$

$$\frac{\partial \Phi}{\partial \sigma_{\text{eq}}} = \frac{2\sigma_{\text{eq}}}{\bar{\sigma}_0^2}$$

$$\frac{\partial \Phi}{\partial H_1} = -\frac{\bar{\sigma}_0'}{\sigma_y^2}\left[2\frac{\sigma_{\text{eq}}^2}{\bar{\sigma}_0} + 3q_1 q_2 f^*(f)\sigma_m \sinh\left(\frac{3q_2\sigma_m}{2\sigma_y}\right)\right]$$

$$\frac{\partial \Phi}{\partial H_2} = 2\frac{\partial f^*(f)}{\partial f}\left[q_1 \cosh\left(\frac{3q_2\sigma_m}{2\sigma_y}\right) - q_3 f^*(f)\right]$$

$$\frac{\partial^2 \Phi}{\partial \sigma_m \partial H_1} = -\frac{3q_1 q_2 f^*(f)\bar{\sigma}_0'}{\bar{\sigma}_0^2}\left(\sinh\left(\frac{3q_2\sigma_m}{2\bar{\sigma}_0}\right) + \frac{3q_2\sigma_m}{2\bar{\sigma}_0}\cosh\left(\frac{3q_2\sigma_m}{2\bar{\sigma}_0}\right)\right)$$

$$\frac{\partial^2 \Phi}{\partial \sigma_m \partial H_2} = \frac{3q_1 q_2}{\bar{\sigma}_0}\frac{\partial f^*(f)}{\partial f} \sinh\left(\frac{3q_2\sigma_m}{2\sigma_y}\right)$$

$$\frac{\partial^2 \Phi}{\partial \sigma_{\mathrm{eq}} \partial H_1} = \frac{-4\sigma_{\mathrm{eq}}}{\bar{\sigma}_0^3} \bar{\sigma}_0'$$

$$\frac{\partial^2 \Phi}{\partial \sigma_{\mathrm{eq}} \partial H_2} = 0$$

$$\frac{\partial f^*(f)}{\partial f} = \begin{cases} 1 & \text{for } f \leqslant f_c \\ \frac{1/q_1 - f_c}{f_f - f_c} & \text{for } f > f_c \end{cases}$$

where $\bar{\sigma}_0'$ is the derivative of true stress versus natural strain from a tensile test, $\bar{\sigma}_0' = \partial \bar{\sigma}_0(\bar{\varepsilon}^{\mathrm{pl}})/\partial \bar{\varepsilon}^{\mathrm{pl}}$.

The derivatives $\partial H_i/\partial D_m$ and $\partial H_i/\partial D_{\mathrm{eq}}$ are obtained in the following way. The time derivatives of H_1 and H_2 are

$$\dot{H}_1 = h_1(D_m, D_{\mathrm{eq}}, \sigma_m, \sigma_{\mathrm{eq}}, H_1, H_2)$$

$$\dot{H}_2 = h_2(D_m, D_{\mathrm{eq}}, \sigma_m, \sigma_{\mathrm{eq}}, H_1, H_2)$$

Since these rates are assumed to be constant during the time step from $t = t_n$ to $t = t_{n+1} = t_n + \Delta t$, the linearized behaviour around $t = t_n$ can be written as

$$H_i(t = t_n + \Delta t) = H_{i,n+1} = H_{i,n} + \Delta t h_i(D_m, D_{\mathrm{eq}}, \sigma_m, \sigma_{\mathrm{eq}}, H_i) \tag{A18}$$

Taking the derivative of Equation (A17) with respect to D_m gives the two equations

$$\frac{\partial H_1}{\partial D_m} = \Delta t \left(\frac{\partial h_1}{\partial D_m} + \frac{\partial h_1}{\partial \sigma_m} \frac{\partial \sigma_m}{\partial D_m} + \frac{\partial h_1}{\partial H_1} \frac{\partial H_1}{\partial D_m} + \frac{\partial h_1}{\partial H_2} \frac{\partial H_2}{\partial D_m} \right)$$

$$\frac{\partial H_2}{\partial D_m} = \Delta t \left(\frac{\partial h_2}{\partial D_m} + \frac{\partial h_2}{\partial \sigma_m} \frac{\partial \sigma_m}{\partial D_m} + \frac{\partial h_2}{\partial H_1} \frac{\partial H_1}{\partial D_m} + \frac{\partial h_2}{\partial H_2} \frac{\partial H_2}{\partial D_m} \right)$$

Noting that $\partial \sigma_m/\partial D_m = -K \Delta t$ and writing in matrix form give

$$\begin{Bmatrix} 1 - \Delta t \frac{\partial h_1}{\partial H_1} & -\Delta t \frac{\partial h_1}{\partial H_2} \\ -\Delta t \frac{\partial h_2}{\partial H_1} & 1 - \Delta t \frac{\partial h_2}{\partial H_2} \end{Bmatrix} \begin{Bmatrix} \frac{\partial H_1}{\partial D_m} \\ \frac{\partial H_2}{\partial D_m} \end{Bmatrix} = \Delta t \begin{Bmatrix} \frac{\partial h_1}{\partial D_m} - \Delta t K \frac{\partial h_1}{\partial \sigma_m} \\ \frac{\partial h_2}{\partial D_m} - \Delta t K \frac{\partial h_2}{\partial \sigma_m} \end{Bmatrix} \tag{A19}$$

Following a derivation as above, the derivatives $\partial H_i/\partial D_{\mathrm{eq}}$ are given by the system of equations

$$\begin{Bmatrix} 1 - \Delta t \frac{\partial h_1}{\partial H_1} & -\Delta t \frac{\partial h_1}{\partial H_2} \\ -\Delta t \frac{\partial h_2}{\partial H_1} & 1 - \Delta t \frac{\partial h_2}{\partial H_2} \end{Bmatrix} \begin{Bmatrix} \frac{\partial H_1}{\partial D_{\mathrm{eq}}} \\ \frac{\partial H_2}{\partial D_{\mathrm{eq}}} \end{Bmatrix} = \Delta t \begin{Bmatrix} \frac{\partial h_1}{\partial D_{\mathrm{eq}}} - 3\Delta t G \frac{\partial h_1}{\partial \sigma_{\mathrm{eq}}} \\ \frac{\partial h_2}{\partial D_{\mathrm{eq}}} - 3\Delta t G \frac{\partial h_2}{\partial \sigma_{\mathrm{eq}}} \end{Bmatrix} \tag{A20}$$

Finally, the partial derivatives in Equations (A19), (A20) are given by

$$H_1 = \bar{\varepsilon}^{\mathrm{pl}}$$

$$H_2 = f$$

$$\dot{H}_1 \equiv h_1 = \frac{\sigma_m D_m + \sigma_{\mathrm{eq}} D_{\mathrm{eq}}}{(1-f)\sigma_y}$$

$$\dot{H}_2 \equiv h_2 = (1-f)D_m + B_{\mathrm{GTN}}\dot{\bar{\varepsilon}}^{\mathrm{pl}}$$

$$A_{\mathrm{N}} = \frac{f_n}{s_n \sqrt{2\pi}} \exp\left[-\frac{1}{2}\left(\frac{\bar{\varepsilon}^{\mathrm{pl}} - \varepsilon_n}{s_n}\right)^2\right]$$

$$\frac{\partial h_1}{\partial H_1} = -\frac{h_1}{\bar{\sigma}_0}\bar{\sigma}'_0$$

$$\frac{\partial h_2}{\partial H_1} = A_{\mathrm{N}}\left[\frac{\partial h_1}{\partial H_1} - \frac{(\bar{\varepsilon}^{\mathrm{pl}} - \varepsilon_n)h_1}{s_n^2}\right]$$

$$\frac{\partial h_1}{\partial H_2} = \frac{h_1}{(1-f)}$$

$$\frac{\partial h_2}{\partial H_2} = -D_m + A_{\mathrm{N}}\frac{\partial h_1}{\partial H_2}$$

$$\frac{\partial h_1}{\partial \sigma_m} = \frac{D_m}{(1-f)\bar{\sigma}_0} \quad \frac{\partial h_2}{\partial \sigma_m} = A_{\mathrm{N}}\frac{\partial h_1}{\partial \sigma_m}$$

$$\frac{\partial h_1}{\partial \sigma_{\mathrm{eq}}} = \frac{D_{\mathrm{eq}}}{(1-f)\bar{\sigma}_0} \quad \frac{\partial h_2}{\partial \sigma_{\mathrm{eq}}} = A_{\mathrm{N}}\frac{\partial h_1}{\partial \sigma_{\mathrm{eq}}}$$

$$\frac{\partial h_1}{\partial D_m} = \frac{\sigma_m}{(1-f)\bar{\sigma}_0} \quad \frac{\partial h_2}{\partial D_m} = (1-f) + A_{\mathrm{N}}\frac{\partial h_1}{\partial D_m}$$

$$\frac{\partial h_1}{\partial D_{\mathrm{eq}}} = \frac{\sigma_{\mathrm{eq}}}{(1-f)\bar{\sigma}_0}$$

$$\frac{\partial h_2}{\partial D_{\mathrm{eq}}} = A_{\mathrm{N}}\frac{\partial h_1}{\partial D_{\mathrm{eq}}}$$

REFERENCES

1. Hancock JW, Reuter WG, Parks DM. Constraint and toughness parameterized by T. *Constrain Effects in Fracture*, *ASTM STP* 1993; **1171**:21–40.
2. Anderson TL. *Fracture Mechanics—Fundamentals and Applications* (2nd edn). CRC Press: Boca Raton, FL, 1995.
3. ODowd NP, Shih CF. Family of crack-tip fields characterized by a triaxiality parameter—I. Structure and fields. *Journal of the Mechanics and Physics of Solids* 1991; **39**:898–1015.
4. Rice JR, Tracey DM. On the ductile enlargement of voids in triaxial stress fields. *Journal of the Mechanics and Physics of Solids* 1969; **17**:201–217.
5. McClintock FA. A criterion for ductile fracture by the growth of holes. *Journal of Applied Mechanics* 1968; **35**:363–371.
6. Gurson AL. Continuum theory of ductile rupture by void nucleation and growth: part 1—yield criteria and flow rules for porous ductile media. *ASME Journal of Engineering Materials and Technology* 1977; **99**.
7. Tvergaard V. Influence of voids on shear band instabilities under plane strain condition. *International Journal of Fracture Mechanics* 1981; **17**:389–407.
8. Tvergaard V. On localization in ductile materials containing spherical voids. *International Journal of Fracture* 1982; **18**:237–252.
9. Tvergaard V. Needleman A. Analysis of the cup–cone fracture in a round tensile bar. *Acta Metallurgica* 1984; **32**:157–169.
10. Pardoen T. Hutchinson JW. An extended model for void growth and coalescence. *Journal of the Mechanics and Physics of Solids* 2000; **48**:2467–2512.
11. Roychowdhury S, Roy YDA, Dodds Jr RH. Ductile tearing in thin aluminum panels: experiments and analysis using large displacement, 3-d surface cohesive elements. *International Journal of Solids and Structures* 2002; **69**:983–1002.
12. Besson J, Steglich D, Brocks W. Modelling of crack growth in round bars and plane strain specimens. *International Journal of Solids and Structures* 2001; **38**:8259–8284.
13. Xia L, Shih F, Hutchinson JW. A computational approach to ductile crack growth under large scale yielding conditions. *Journal of the Mechanics and Physics of Solids* 1995; **43**(3):389–413.
14. Rashid MM. The arbitrary local mesh replacement method: an alternative to remeshing for crack propagation analysis. *Computer Methods in Applied Mechanics and Engineering* 1996; **154**:133–150.
15. Wells GN, Sluys LJ. A new method for modelling cohesive cracks using finite elements. *International Journal for Numerical Methods in Engineering* 2001; **50**:2667–2682.
16. Moes N, Belytschko T. Extended finite element method for cohesive crack growth. *Engineering Fracture Mechanics* 2002; **68**:813–833.
17. Lucy LB. A numerical approach to the testing of the fission hypothesis. *Astrophysical Journal* 1977; **82**:1013–1024.
18. Gingold RA, Monoghan JJ. Smoothed particle hydrodynamics: theory and application to non-spherical stars. *Monthly Notices of the Royal Astronomical Society* 1977; **181**:375–389.
19. Li S, Liu W-K. *Particle Methods* (1st edn). Springer: Berlin, 2004.
20. Belytschko T, Krongauz Y, Organ D, Fleming M, Krysl P. Meshless methods: an overview and recent developments. *Computer Methods in Applied Mechanics and Engineering* 1996; **139**:3–47.
21. Li S, Liu W-K. Meshfree and particle methods and their applications. *Applied Mechanics Review* 2002; **55**(1):1–34.
22. Liu W-K, Li S, Belytschko T. Moving least-square reproducing kernel methods: (i) methodology and convergence. *Computer Methods in Applied Mechanics and Engineering* 1997; **143**:113–154.
23. Belytschko T, Liu W-K, Moran B. *Nonlinear Finite Elements for Continua and Structures* (1st edn). Wiley; New York, 2001.
24. Li S, Liu W-K. Numerical simulations of strain localization in inelastic solids using mesh-free methods. *International Journal for Numerical Methods in Engineering* 2000; **48**:1285–1309.
25. Li S, Hao W, Liu W-K. Mesh-free simulations of shear banding in large deformation. *International Journal of Solids and Structures* 2000; **37**:7185–7206.
26. Li S, Hao W, Liu W-K. Numerical simulations of large deformation of thin shell structures using meshfree methods. *Computational Mechanics* 2000; **25**:102–116.
27. Belytschko T, Krongauz Y, Fleming M, Organ D, Liu W-K. Smoothing and accelerated computations in the element free Galerkin method. *Journal of Computational and Applied Mathematics* 1996; **74**:111–126.

28. Fleming M, Chu YA, Moran B, Belytschko T. Enriched element-free Galerkin methods for crack tip fields. *International Journal for Numerical Methods in Engineering* 1997; **40**:1483–1504.

29. Mathur KK, Needleman A, Tvergaard V. Three dimensional analysis of dynamic ductile crack growth in a thin plate. *Journal of the Mechanics and Physics of Solids* 1996; **44**:439–469.

30. Baaser H, Gross D. Crack analysis in ductile cylindrical shells using Gurson's model. *International Journal of Solids and Structures* 2000; **37**:7093–7104.

31. Simonsen BC, Törngvist R. Experimental and numerical modelling of ductile crack propagation in large-scale shell structures. *Marine Structures*, 2004; accepted for publication.

32. Krysl P. Belytschko T. The element free Galerkin method for dynamic propagation of arbitrary 3-D cracks. *International Journal for Numerical Methods in Engineering* 1999; **44**:767–800.

33. Aravas N. On the numerical integration of a class of pressure-dependent plasticity models. *International Journal for Numerical Methods in Engineering* 1987; **24**:1395–1416.

34. Hao S, Liu W-K, Chang CT. Computer implementation of damage models by finite element and meshfree methods. *Computer Methods in Applied Mechanics and Engineering* 2000; **187**:401–440.

35. Hughes TJR, Winget J. Finite rotation effects in numerical integration of rate constitutive equations arising in large-deformation analysis. *International Journal for Numerical Methods in Engineering* 1980; **15**:1862–1867.

36. Chu CC, Needleman A. Void nucleation effects in biaxially stretched sheets. *Journal of Engineering Materials and Technology* 1980; **102**:249–256.

37. Tvergaard V. Material failure by void growth to coalescence. *Advances in Applied Mechanics* 1990; **27**: 83–151.

38. Roy YA, Dodds Jr RH. Simulation of ductile crack growth in thin aluminum panels using 3-d surface cohesive elements. *International Journal of Fracture* 2001; **110**:21–45.

39. Yu X. Structural analysis with large deformations up to fracture and with dynamic failure. *Ph.D. Thesis*, Hamburg University, 1996 (in German).

40. Xia L, Shih F. Ductile crack growth—I. A numerical study using computational cells with microstructurally—based length scales. *Journal of the Mechanics and Physics of Solids* 1995; **43**(2):233–259.

41. Xia L, Shih F. Ductile crack growth—II. Void nucleation and geometry effects on macroscopic fracture behaviour. *Journal of the Mechanics and Physics of Solids* 1995; **43**(12):1953–1981.

42. Mikkelsen LP. Post-necking behaviour modelled by a gradient dependent plasticity theory. *International Journal of Solids and Structures* 1997; **34**:4532–4546.

43. Joyce JA, Hacket EM. Development of an engineering definition of the extent of J-controlled crack growth. In *Defect Assessment of Components—Fundamentals and Application*, ESIS/EGF9, Blaut JG, Schwalbe KH. (eds). Mechanical Engineering Publications: London, 1994; 233–249

44. Joyce JA, Link RE. Effects of constraint on upper shelf fracture toughness. *Fracture Mechanics* In Newman Jr JC, Reuter WG, Underwood JH (eds), *26th vol.*, *ASTM STP 1256*. American Society for Testing Materials: 1994.